Quantitative microstructure analysis for solid-state metal additive manufacturing via deep learning

Article *in* Journal of Materials Research · June 2020

DOI: 10.1557/jmr.2020.120

CITATIONS
11

READS
735

4 authors:

Yi Han
Virginia Polytechnic Institute and State University
1 PUBLICATION **11** CITATIONS
SEE PROFILE

R. Joey Griffiths
Virginia Polytechnic Institute and State University
13 PUBLICATIONS **285** CITATIONS
SEE PROFILE

Hang Yu
Virginia Polytechnic Institute and State University
41 PUBLICATIONS **663** CITATIONS
SEE PROFILE

Yunhui Zhu
Virginia Polytechnic Institute and State University
48 PUBLICATIONS **384** CITATIONS
SEE PROFILE

Journal of MATERIALS RESEARCH

Article
DOI: 10.1557/jmr.2020.120

Quantitative microstructure analysis for solid-state metal additive manufacturing *via* deep learning

Yi Han[1], R. Joey Griffiths[2], Hang Z. Yu[2], Yunhui Zhu[1,a)]

[1]*Bradley Department of Electrical and Computer Engineering, Virginia Tech, Blacksburg, Virginia 24061, USA*
[2]*Department of Materials Science and Engineering, Virginia Tech, Blacksburg, Virginia 24061, USA*
[a)]Address all correspondence to this author. e-mail: yunhuiz@vt.edu

Received: 13 January 2020; accepted: 27 April 2020

Metal additive manufacturing (AM) provides a platform for microstructure optimization *via* process control, but establishing a quantitative processing-microstructure linkage necessitates an efficient scheme for microstructure representation and regeneration. Here, we present a deep learning framework to quantitatively analyze the microstructural variations of metals fabricated by AM under different processing conditions. The principal microstructural descriptors are extracted directly from the electron backscatter diffraction patterns, enabling a quantitative measure of the microstructure differences in a reduced representation domain. We also demonstrate the capability of predicting new microstructures within the representation domain using a regeneration neural network, from which we are able to explore the physical insights into the implicitly expressed microstructure descriptors by mapping the regenerated microstructures as a function of principal component values. We validate the effectiveness of the framework using samples fabricated by a solid-state AM technology, additive friction stir deposition, which typically results in equiaxed microstructures.

INTRODUCTION

The last decade has witnessed waves of advances in metal additive manufacturing (AM), from the popularly used beam-based technologies, such as powder bed fusion and directed energy deposition [1], to the more emerging solid-state technologies such as ultrasonic AM [2] and additive frictions stir deposition [3, 4]. Given the far-from-equilibrium processing conditions in most metal AM, the microstructure in the as-printed material is dictated by the processing kinetics and is sensitively dependent on the processing parameters [1, 3, 5, 6]. Typically involving a significant number of tunable processing parameters and therefore a large processing space [1, 7], metal AM does not only unlock the freedom in 3D shaping with complex geometries but also allows for microstructure design in the as-printed components, from which the mechanical properties can be controlled. Unfortunately, achieving the desired microstructure by AM parameter optimization is still mostly a trial-and-error process, which is slow and expensive.

With metal AM providing an optimal platform for microstructure control through processing, establishment of a quantitative processing-microstructure linkage is essential for microstructure optimization per given applications. However, such an establishment is impossible without an efficient scheme for quantitative description of the microstructures resulting from metal AM. The microstructure of a polycrystalline material is traditionally described by imaging-based qualitative interpretation. This relies on characterization techniques such as optical microscopy, electron microscopy, and most representatively electron backscatter diffraction (EBSD), which provides orientation and positional information of individual grains [8]. Recently, simple quantitative microstructure descriptions based on the EBSD patterns have become widespread in material research, wherein pre-defined microstructure descriptors, such as average grain size, grain size deviation, micro-texture, grain boundary misorientation distribution, and other features, are quantitatively analyzed [8, 9, 10]. There is no doubt that this type of description can provide important information of the microstructure, but it is insufficient in two critical aspects. First, the selection of the pre-defined microstructure descriptors is arbitrary; it is not guaranteed that they can comprehensively or efficiently represent the essence of any given microstructure. Second, the quantification is based on statistical homogenization and distribution functions, so location-dependent microstructure

information is not effectively preserved. To address these problems, more sophisticated microstructure representation approaches have been proposed, including Hyperspherical harmonics [11, 12], network representation and spectral graphic theory [13], and *n*-point correlation functions [14]. It has also been proposed to register the complete geometry information for each grain using microstructure basis functions in the rotational grain boundary space [15, 16].

Fundamentally, the challenges in microstructure representation lie in the processing and analysis of the high-dimensional data describing the microstructure as well as the identification of the principal descriptors that most effectively represent the microstructural features or variations for a given problem. It is important to note that the principal microstructure descriptors may differ case by case, depending on the goal of the target problem—e.g., whether it is to identify the most salient feature changes by varying processing parameters, or to recognize the most influential features that control the yield strength or the fracture toughness. With the advance and resurgence of artificial intelligence, new opportunities arise in terms of resolving the microstructure representation problem using data-driven approaches in addition to the conventional physics-based approaches. This strategy is promising as the data-driven approaches have been proven effective for big-data analytics and feature extraction [17, 18, 19, 20]. In particular, deep learning [21] has emerged as a prominent approach for quantitative analysis of high-dimensional data and has demonstrated unprecedented capabilities of identifying multiscale features from complex data patterns. Examples abound in computer vision and data processing, such as image classification [22, 23, 24], semantic segmentation [25], object detection [26, 27, 28], instance segmentation [29], clustering analysis [30, 31, 32], texture synthesis, and reconstruction [33, 34], and computer-aided material design [35, 36, 37]. Deep learning has also been actively applied in EBSD imaging denoizing and indexing [38, 39, 40], wherein the crystal orientation information is extracted from noisy and blurring Kikuchi patterns. Noteworthy recent advancements in deep learning-based image analysis include StyleGan, which is a generative adversarial network that can generate visually indistinguishable fake images from pre-defined attributes [41], as well as PointRend, which is an instance segmentation algorithm with high accuracy and efficiency [42].

Encouraged by the success in feature extraction and image reconstruction, we explore the potential of using deep learning and deep neural networks (DNNs) for microstructure representation and regeneration in metal AM, which is based on the analysis and feature extraction of EBSD patterns (i.e., the inverse pole figure maps). Following Gatys' multilayer pattern representation scheme [34], we present a deep learning framework that extracts the key microstructural features from a pre-trained DNN. Unlike the conventional feature extraction method that only uses the last layer, Gatys' method uses the Gram matrix in multiple layers to permit a multiscale microstructure representation. This framework allows us to examine the microstructure formed under drastically different processing conditions in metal AM and to identify the most distinguishable microstructural features (i.e., microstructure descriptors) using principal component analysis, from which a reduced representation of the microstructure is established. Within the reduced representation domain, possible microstructures are predicted *via* microstructure regeneration through convolutional neural networks [43].

As one of the first attempts to leverage DNN in microstructure representation and regeneration, here we test the framework using samples fabricated by a solid-state metal AM technology, additive friction stir deposition, which is known to result in simple equiaxed grains rather than the complicated dendritic microstructures commonly seen in powder bed fusion and directed energy deposition. We confirm the effectiveness of the resultant microstructure representation and regeneration and discuss the physical insights into the implicitly expressed microstructural descriptors by mapping the regenerated microstructures in the reduced representation domain. This exploratory work lays the foundation toward establishment of quantitative processing-structure linkages in metal AM and can be potentially employed in general materials science problems, such as heterogeneous material design and optimization.

FRAMEWORK OF QUANTITATIVE MICROSTRUCTURE REPRESENTATION *VIA* DEEP LEARNING

Quantitative microstructure analysis based on the EBSD patterns or inverse pole figure maps can be viewed as a quantitative image analysis problem, which has benefited significantly from deep neural networks (DNNs), such as VGG16 [44], Inception [24], and ResNet [23]. These networks are all trained on ImageNet, an extremely large dataset with over 10^6 images from 1000 different classes [45]. With such a large database, the network is able to learn the representative features of the images for successful classification. By taking advantages of the learned representations on the convolutional and fully connected layers, transfer learning can be applied to enable feature extraction in unsupervised machine learning [46] and supervised learning on a small dataset [47]. The special characteristic of EBSD patterns is that the image is "textured"—which, in image processing terms, means that it involves repeated local patterns that are translational invariant. This should be distinguished from the concept of texture in metallurgy, which corresponds to preferred crystallographic orientations in a polycrystal. In the realm of image analysis, the texture

representation scheme developed by Gatys has seen great success in texture synthesis [34] and image style transfer [41] and has been proven to be capable of generating images with astonishingly high similarity [43]. The presented deep learning framework follows the same philosophy of this scheme to analyze the EBSD patterns for microstructure representation and regeneration in metal AM, and in addition uses principal component analysis to extract the microstructural descriptors that represent the differences between the measured microstructures.

Figure 1 shows the overall flowchart of the presented deep learning framework for microstructure representation and regeneration in metal AM, including three major steps. First, an EBSD measurement is implemented on samples processed with drastically different additive friction stir deposition conditions. The measured EBSD patterns are augmented to generate a large dataset for multiscale feature extraction through a pre-trained DNN in Step 2. The Gram matrix is calculated for the last layer on each of the five different scales, yielding a multiscale feature vector. Based on this multiscale feature extraction, a reduced representation is generated *via* principal component analysis (PCA), which maximizes the microstructure differences among samples made by various additive friction stir deposition conditions. Supervised classification is then performed on the reduced representation, which only requires the use of a few principal components. Finally, in Step 3, a regeneration network is established to retrieve the microstructures at given locations within the reduced representation domain. This framework is implemented using Python with Tesonflow [48], Keras [49] and Scikit-Learn [50].

Preprocessing of EBSD data

The dataset of training comes from commercially pure copper fabricated by additive friction stir deposition under different manufacturing conditions [51], which are mainly defined by the tool head rotation rate Ω and in-plane motion velocity V. There are three different sets of processing conditions including Ω = 300 RPM and V = 9 in/min, Ω = 600 RPM and V = 3 in/min, and Ω = 600 RPM and V = 9 in/min. The obtained EBSD patterns (inverse pole figures) are shown in Figs. 2(a)–2(c) with the same field of view and labeled as M1, M2, and M3, respectively [51].

To generate the training data from such a small dataset (only three EBSD orientation maps), we implement a data augmentation procedure. The large microstructure images are cropped into a set of smaller pieces with a scanning window. The size of the cropping window is chosen to be slightly above the scale, where microstructure characteristics can be considered to be uniform. Random horizontal and vertical flip are implemented to further increase the size of training datasets. All cropped images are generated with the same scale and the aspect ratio to maintain the grain size and shape characteristics. The dataset is then randomly split into training and testing sets by the ratio of 8:2.

Multilayer feature extraction from VGG16

The generated training data is then fed into a DNN. In this work, we use a convolutional neural network (VGG16), which was trained on ImageNet to classify natural images [44]. VGG16 is a very deep DNN developed for large-scale

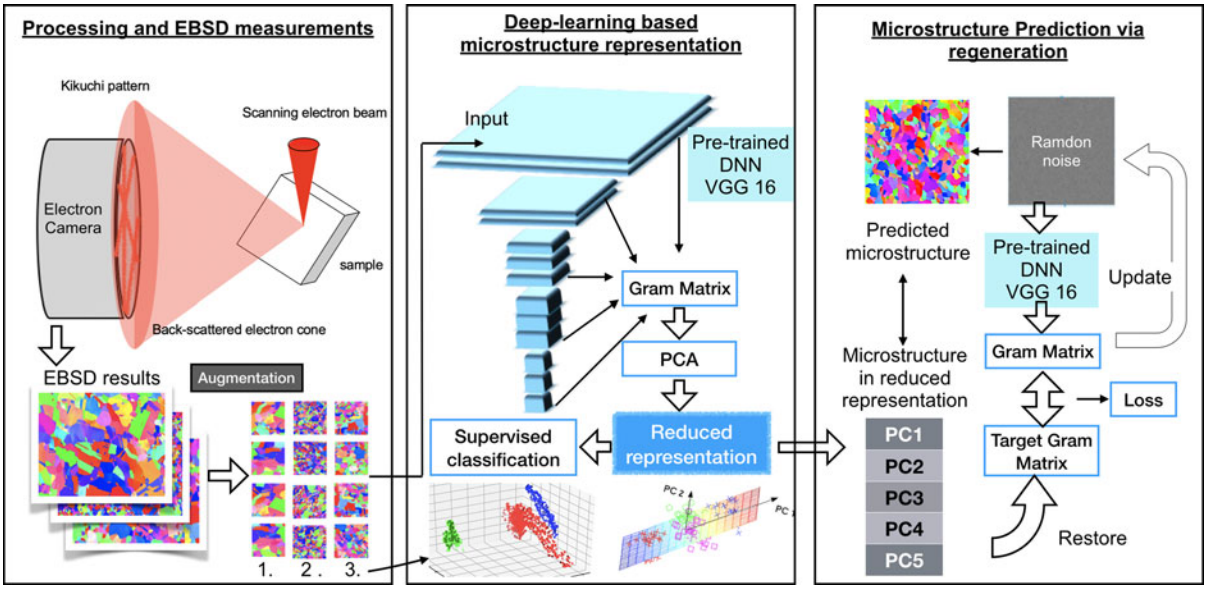

Figure 1: Experimental flowchart. Step 1: Microstructures of the processed samples are measured *via* EBSD. Step 2: Reduced representation is established through PCA analysis using multilayer feature extraction. Step 3: Predictions of microstructures are generated through the restoration of the Gram matrix from designated principal component values.

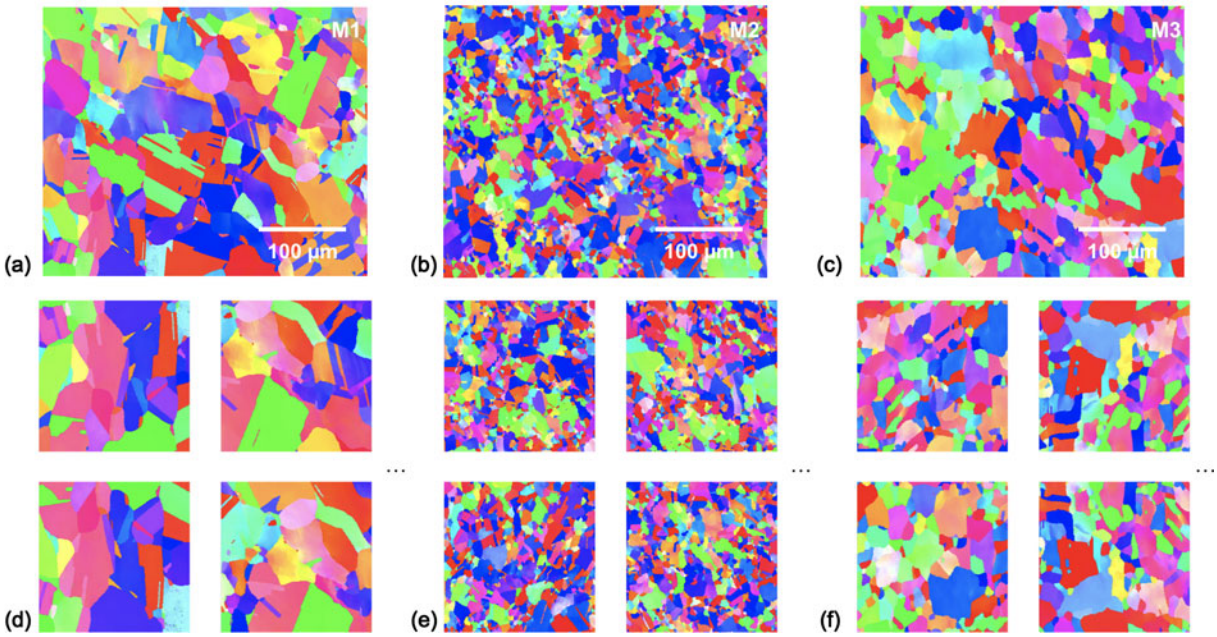

Figure 2: Microstructure measurements from EBSD for three different processing conditions, labeled as (a) M1, (b) M2, and (c) M3, from Ref. [51]. (d–f) show a small subset of randomly augmented patches cropped with a scanning window size of 179 × 179 μm^2 for each microstructure, respectively. Random horizontal and vertical flip are applied to increase the number of data patches.

image recognition tasks and has demonstrated capability of processing and extracting spatial features with very high dimensions. The DNN contains five convolutional blocks that perform convolutional calculations on five different length scales. At the end of each block, a max-pooling layer downsamples the extracted feature map. Normally, activation of the final convolutional layer is used as the extracted feature to identify the object in the image. In our application, however, more emphasis is needed for the statistical correlation of patterns across multiple scales. We apply Gatys's scheme [34] to extract image texture features based on the Gram matrix, where we focus on the pair-wise correlation between feature maps generated on multiple layers of the network. By explicitly including correlation features on each of the five scales of the blocks, the texture feature extraction is proven to be more sensitive to the multiscale patterns. Features are extracted based on the Gram matrix calculated for multiple layers with the following equation:

$$G^l_{ij} = \sum_k F^l_{ik} F^l_{jk},$$

where l denotes the index of the layer, F^l is the matrix that stores the activation of the feature map and filters, i and j are the indices for one pair of feature, F^l_{ik} corresponds to the activation of the ith filter in layer l at position k. Five Gram matrices are calculated from the activation of the last layers from each convolutional block of VGG16. The feature map size generated by the VGG16 for the five blocks are 64, 128, 256, 512, and 512, respectively. After the correlation calculation, the Gram matrices of all five layer contains $64 \times 64 + 128 \times 128 + 256 \times 256 + 512 \times 512 + 512 \times 512 = 610{,}304$ elements. This Gram matrix is flattened as a feature vector and is used in the following analysis.

Reduced microstructure representation

The Gram matrix-based feature vector, while extracting comprehensive correlation information, is cumbersome. Direct classification and visualization analysis based on such high-dimensional data is infeasible. We, thus, perform a principal component analysis (PCA) on the flattened Gram matrix to generate a reduced representation from the training data of the EBSD measurements. The analysis identifies the principal components that maximally preserve the variance between the input microstructures. In this way, PCA can significantly reduce the dimensions of representation by removing the correlated features.

The established principal components (PC) from the training data can be used as basis features to span a reduced representation domain for microstructures. Arbitrary microstructure can be projected into the reduced representation domain by evaluating its Gram matrices from the pre-trained DNN and applying the PCA transform. As a result, the microstructure differences can be quantitatively measured in terms of distances in the PC representation domain.

Note that the reduced PC domain is established to best represent the differences between the microstructures in the

training datasets. It is possible that new microstructure data may contain differences that are not captured by the PCs generated from the training dataset. The effectiveness of the representation can be evaluated by restoring the Gram matrix feature vector from the reduced representation using the PCA inverse transformation process, followed by calculating the fidelity η through the complement of normalized mean square error (NMSE) between the restoration and the ground truth *via*

$$\eta = 1 - \frac{\sum_i (G_i - \hat{G}_i)^2}{\sum_i G_i^2}, \quad (1)$$

where the largest possible value of 1 means full restoration and lower value means worse restoration. If the differences of the new microstructure are well captured by the established PC, we know that the new microstructure is well represented in the reduced domain. On the other hand, a poor NMSE value indicates that the new microstructure involves feature variance on a different dimension and that the established representation needs to be extended.

Classification of microstructures

The established reduced representation is then used to classify microstructure patches for each measurement. Support vector machine (SVM) is proven to be reliable for binary classification, by which a hyperplane is formed to separate the datasets while maximizing the margin of separation [52, 53]. For multiclass classification, one-to-rest strategy can be used to train one binary SVM classifier for each class. In our framework, linear SVM classifiers are trained and validated on the principal features to classify the microstructures from the three processing conditions. The classification accuracy of the SVM has been used as a metric for finding the best number of dimensions to keep. The accuracy is evaluated from 2 to 10 principal components. The number of principal components is chosen at the point where accuracy converges.

Microstructure regeneration based on the reduced representation

While we have demonstrated the approach that reduces the number of microstructural descriptors through PCA, a successful reduced representation also requires that high-dimensional microstructure data be restored from the few-PC based representation. The restoration of the microstructure from the reduced representation is achieved by feature-based image regeneration. We first restore the feature vector from PC by the inverse transform process of PCA. As illustrated in the previous section, the quality of the restoration can be evaluated by the NMSE. Next, the restored Gram matrix feature vector G is used as the target feature map. Following Gatys' style transformation work, an initial random noise image with feature vector $\hat{G}$ is repeatedly updated and optimized to match the restored Gram matrix G. The loss between the Gram matrices is evaluated for each layer*lvia*

$$E^l = \frac{1}{4|F^l|^2} \sum_i (G_i^l - \widehat{G}^l{}_i)^2, \quad (2)$$

where $|F^l|$ denotes the size of F^l. The total loss is summed up for all five layers. A total variation loss [54] is added to the loss function as a regularization term to increase the smoothness of the generated image and suppress noise. Optimization is achieved *via* L-BFGS-B algorithm [55] and back propagation. After a number of iterations, or after the loss converges, the algorithm stops and the output of the updated image resembles the predicted microstructure for the given data point in the PC domain. This method allows us not only to regenerate microstructures similar to the input EBSD measurements but also to generate "in-between" microstructures with a set of in-between PC values. In this way, we can predict new microstructures at arbitrary locations within the PC domain. Note that in Gatys' original work, one can generate an image with a similar Gram matrix from an image. In our case, the Gram matrix is extracted directly from the image or restored from the PC representation.

RESULTS AND DISCUSSION

Microstructure characterization *via* EBSD

The obtained EBSD patterns from the three samples for data training are shown in Figs. 2(a)–2(c). All three microstructures demonstrate clear equiaxed grain shapes that typically result from thermomechanical processing, while exhibiting multiple scale features. On a small length scale, it is evident that there are many grains of various sizes, orientations, and lattice distortion, the latter of which is noted by color gradients within a single grain. At a large length scale, these patterns repeat themselves to some extent. To compare, conditions M1 and M3 have produced relatively large grains with minimal stored internal energy. M1 is notable for having prominent twin boundaries, and low lattice distortion within individual color-gradient grains. Condition M2 results in much smaller grains than the majority of those produced by M1 and M3.

These EBSD images are cropped and flipped to generate a large dataset for each of the microstructure. Four random patches from the generated dataset [Figs. 2(d)–2(f)] are shown for each of the microstructures, respectively. The cropping window size of 179 μm × 179 μm is chosen to avoid local fluctuations and incomplete grain sampling. The symmetric characteristics of the microstructures allows us to flip the patches to increase the size of the training data. According to

the original sizes of the EBSD images, a total number of 315, 448, and 1038 patches are generated for M1, M2, and M3, respectively. 80% of the generated patches are used as training data to extract the multiscale features, while 20% of the patch data are used for testing.

Reduced representation of microstructure

The patch data shown in Figs. 2(d)–2(f) is then processed through the pre-trained DNN network. A multiscale feature vector is generated *via* calculating the correlation Gram matrix on each of the five layers. In this way, we capture the statistical features of the microstructure pattern across various different length scales. As discussed earlier, this Gram matrix-based feature vector contains 610,304 components. Most of these components represent the common features shared by all EBSD orientation maps, which are not of interest for the analysis of microstructure variations in material processing. Instead, the feature components that represent the differences between the measured microstructures are of interest. Such a reduced representation is generated through the PCA analysis illustrated in Sec. II.D, which identifies the principal components (i.e., microstructural descriptors) that are responsible for the variances among the input data patches from the three different microstructures (M1, M2, and M3). Efficiency of the representation is evaluated by the capability of classifying different microstructures from the testing data patches. As shown in Fig. 3(a), the classification achieves near 100% accuracy with merely five principal components, indicating that the differences in the detected microstructures can be represented with a dramatically reduced number of microstructural descriptors. Figure 3(c) shows a visualization of clustering for the sample data points in the 3D space spanned by the first three PCs in the 5PC domain, where training data and testing data are represented by bright and dark colors, respectively. Clear clustering is observed for the three microstructures. In addition, all of the test data are correctly categorized into the corresponding cluster, as shown in the confusion matrix in Fig. 3(b). The PC values at the centroid location for the M1, M2, and M3 clusters are summarized in Table I.

The generated principal components span a continuous 5D space that can be used to represent microstructures beyond the training datasets. In particular, this representation can be used to characterize "in-between" microstructures and quantify the differences with the input microstructures. This capability is especially important for future works on processing-structure modeling. To demonstrate this point, we introduce two new microstructures and characterize them with the established 5PC representation. One EBSD microstructure is obtained from a Cu sample fabricated using additive friction stir deposition, but with a different processing condition ($\Omega = 300$ RPM and $V = 3$ in/min). This new microstructure is labeled as M4 and its EBSD measurement is shown in Fig. 4(a). A similar cropping process is implemented to generate a series of EBSD data patches with the same size as the training data. By processing the patches from M4 through the established neural network and calculating the Gram matrix and its principal components, we are able to locate the new microstructure in the established 5PC space. It is found that the Gram matrix for M4 is well represented by the five principal components, with an NMSE score $\eta = 0.9909$. As shown in the projection 3D plot in Fig. 4(b), the new microstructure is clustered between M1 and M3 and is relatively far from M2. This quantitative analysis result is consistent with the qualitative observation; M4 is visually more similar to M1 and M3. The centroid location for M4 patches in the 5PC domain is calculated with the PC values shown in Table II.

On the other hand, dramatically different microstructures can be identified as outliers. We characterize another EBSD microstructure pattern obtained from Al samples fabricated using additive friction stir deposition ($\Omega = 200$ RPM and $V =$ 3 in/min). The elongated grain shapes in the Al data, shown in Fig. 4(c), are significantly different from the equiaxed Cu data. Such microstructure differences originate from different levels of stacking fault energy and dynamic recovery capability, which is elaborated in a separate work [51]. In consistency with the observation, the Al cluster is located far away from all Cu microstructure clusters [Fig. 4(d)]. The NMSE score for the Al data also decreases drastically, yielding $\eta = 0.9572$. In other words, $1 - \eta$ increases from 0.0091 for Cu to 0.428 for Al. This indicates that the current training data from Cu may not be sufficient to represent the outlier of Al. Re-training should be considered when the fidelity drops significantly with the inclusion of new data, indicating a poor representation of the new microstructure. In our case, re-training is needed for the added Al data. Al and Cu have different microstructure evolution mechanisms during solid-state AM, so the microstructures are characterized by different microstructural descriptors.

Regeneration of microstructures

In the previous section, we demonstrate the reduced representation of the EBSD microstructure patterns in the five-dimensional PC representation domain. Here, we demonstrate the reverse process of generating new microstructure patterns from the 5PC representation. The regeneration is demonstrated for both the measured microstructures as well as the new "in-between" microstructures.

We first regenerate microstructures for the measured microstructures M1, M2, and M3. These regenerations are implemented by matching the generated Gram matrix G^I to

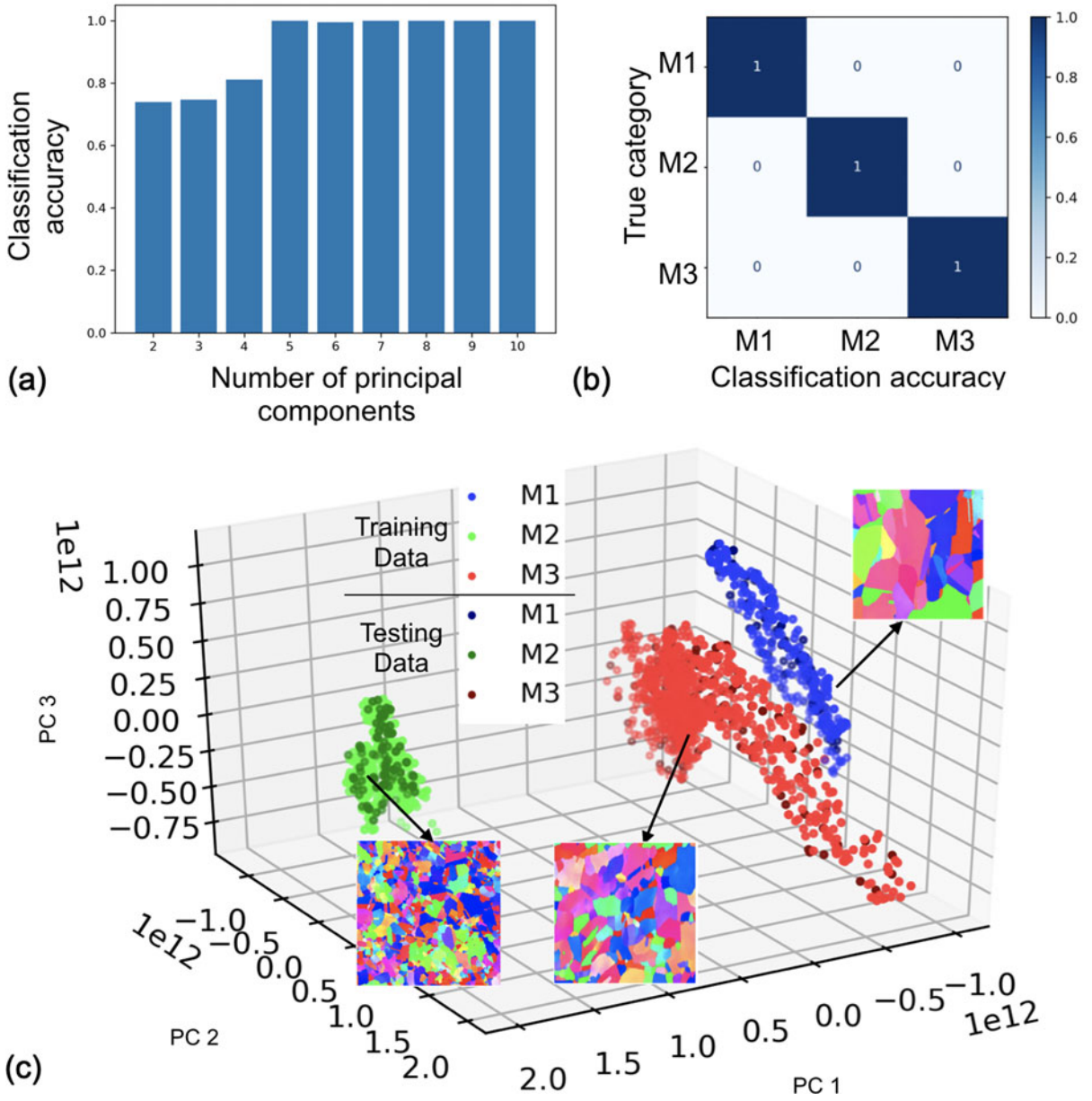

Figure 3: PCA and classification results. (a) Classification accuracy as a function of the number of principal components kept. Near 100% of accuracy is achieved with five principal components, demonstrating the efficiency of the deep learning-based EBSD microstructure representation. (b) Confusion matrix shows the perfect classification results with 5PC. (c) Scattering plot of patch data projected in the reduced domain of the first three principal components. Clear clustering can be observed for patches cropped from different microstructure measurements.

the measured Gram matrix G *via* Eq. 2. Figure 5 shows the regenerated microstructures for M1, M2, and M3, respectively. We can visually observe the similarities of grain size and orientation (color) distribution between the original measurements and the regeneration results. Note that the regeneration described in Sec. II.E is a stochastic process that aims to match the statistical multiscale correlation features. As a result, the regeneration procedure will produce microstructures with random variations for each generated image. These random variation details, however, are not considered to influence the key characteristics of the microstructure. As shown in Fig. 5, the regenerated microstructures R1, R2, and R3 have generally reserved the features of the experimental measurements M1, M2, and M3. In particular, the grain sizes are observed to be similarly distributed, and the color tones which represent the grain orientations have also resembled their origins. Figure 6 shows the predicted microstructures at arbitrary locations in the representation 5PC domain. Three nonexistent microstructures (R4, R5, and R6) are predicted at the centroid location of M4, between M1 and M3, and between M2 and M3,

TABLE I. The PC values for the centroid of M1, M2, and M3.

Indexing	PC1 (10^{11})	PC2 (10^{11})	PC3 (10^{11})	PC4 (10^{11})	PC5 (10^{11})
M1 centroid	−8.021	4.245	4.083	0.6232	2.448
M2 centroid	17.790	0.418	0.105	0.135	0.328
M3 centroid	−5.352	−1.418	−1.174	−0.242	−0.814

respectively. While R4, R5, and R6 are regenerated virtual microstructures, they resemble the experimentally processed microstructures obtained in AFSD. In particular, R4 can be compared with M4, with the similar grain sizes and color distributions, despite the fact that M4 is not included in the training data, and thus cannot influence the regeneration of R4. This proves the accuracy and uniqueness of the established 5PC representation.

Physics interpretation of the representation results

The 5PC representation is highly efficient and accurate to characterize and simulate microstructures for the chosen metal AM of additive friction stir deposition. However, using the presented deep learning framework, the principal microstructural descriptors, i.e., the principal components, are implicitly expressed. To explore the physics insights into the principal components for microstructure representation, we study the trend of the regenerated microstructures with varying PC values (Table III). As shown in Fig. 7, microstructures are regenerated by sequentially stepping along the PC1, PC2, and PC3 axes, respectively. Each row consists of five microstructures. The center one is regenerated at the centroid location of M3, while others are regenerated by decreasing or increasing the PC value with one unit step (the 2nd and 4th in the row) or two unit steps (the 1st and 5th in the row).

As shown in the 1st row, it appears that PC1, the most important feature component, is mostly associated with the grain size. The larger PC1 values correspond to smaller grain sizes. PC2 appears to be associated with the color distribution of the EBSD pattern, which corresponds to the crystallographic orientation distribution of the microstructure. The increase of PC2 changes the microstructure orientation from purple and red to bright green. On the other hand, PC3 gradually changes from light green to dark blue. PC2 and PC3 are, thus, likely to

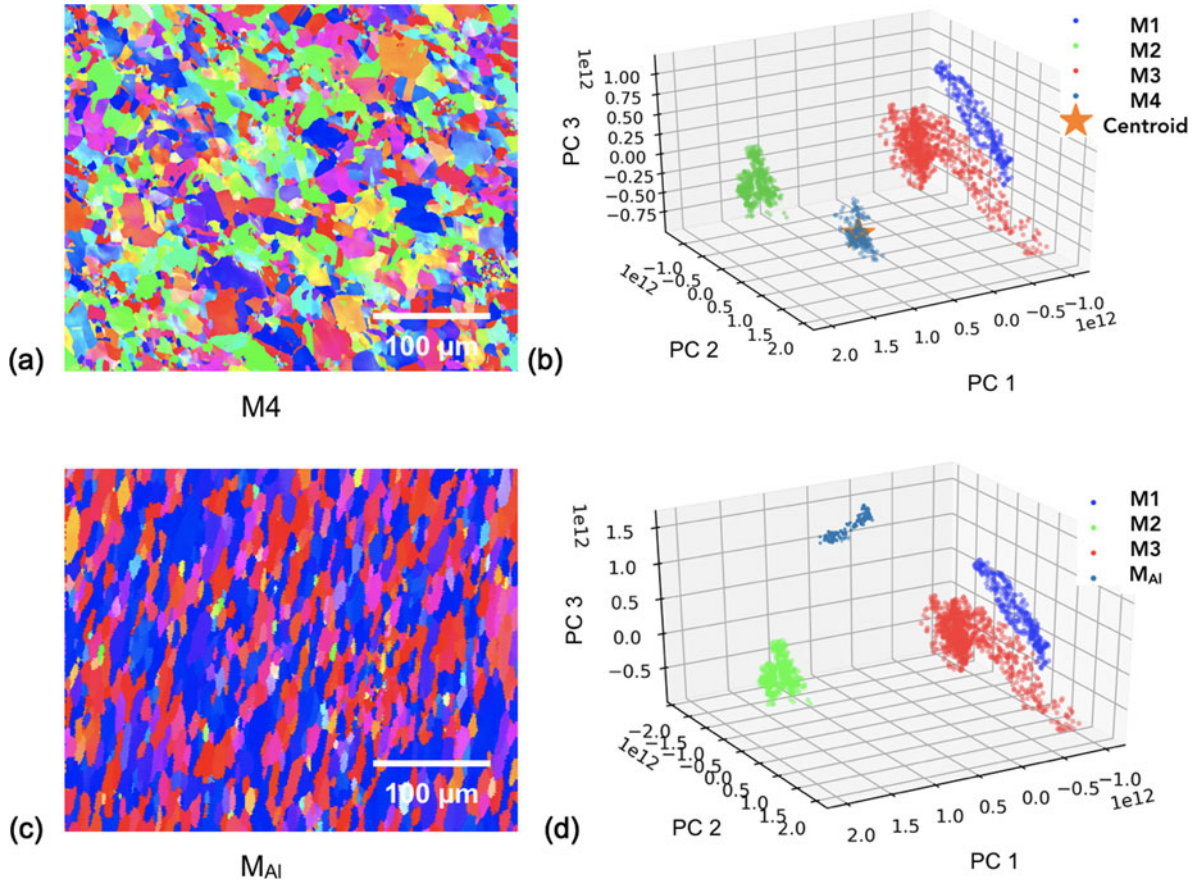

Figure 4: Projection of new microstructures into the 5PC representation domain. (a) EBSD measurement of a Cu sample processed at a new processing condition (M4), from Ref. [51]. (b) The projected dots for cropped patches from M4 and their averaged centroid location. (c) EBSD measurement of an Al sample (M_{Al}), from Ref. [51]. (d) The projected dots for cropped patches from M_{Al}. The result indicates that M4 is similar to M2 and M3, while M_{Al} is not close to any of the input microstructures.

TABLE II. The PC values for the centroid of M4.

Indexing	PC1 (10^{11})	PC2 (10^{11})	PC3 (10^{11})	PC4 (10^{11})	PC5 (10^{11})
M4/R4	9.086	7.893	−5.691	2.793	0.962

be two orthogonal orientation descriptors, representing a set of orthogonal angles or their linear combinations from the 3D Euler angles for crystal orientation. Furthermore, the increase of PC2 and PC3 introduces more straight grain boundary segments. Therefore, PC2 and PC3 should correspond to the crystallographic orientation and grain boundary morphology of the microstructure.

Limitations of microstructure regeneration in this work

The regenerated and newly created EBSD maps (R1–R6) appear fairly realistic and in line with typical maps collected from real samples. Grains appear roughly rounded and vary in size according to their parent condition. Even the color gradient visualization of lattice distortion has been preserved in the regenerations, with R4 showing it clearly in a number of its grains. The deep learning network can identify features from EBSD images regardless of their underlying physical origins. Possible regeneration artifacts, however, may stir from the encoding scheme based on the Gram matrix. Such a pixel–pixel correlation scheme has been demonstrated to represent the texture pattern with high fidelity, but it is less sensitive to nonstatistical features, such as large-scale shapes. In our attempt, it does appear to perform less ideal for M1 with larger grain sizes, and it also misses the occasional twinning.

To improve microstructure regeneration in future works, most notably, quantitative measures on regeneration qualities must be implemented. While the regeneration approach produces realistic orientation maps, the accuracy of these maps is not yet quantified, and important information such as misorientation across a grain boundary remains to be extracted from the newly generated images. These challenges originate from the color coding of inverse pole figure maps (i.e., the colored EBSD patterns), which is based on the function of rotation referenced to a user assigned direction. While it is straightforward to convert the grain orientation into the referenced rotation, it requires at least two sets of rotational angles from orthogonal reference directions to fully retrieve the grain orientation based on color patterns. In other words, the 3D orientation information (i.e., Euler angles) is not fully preserved in the two-dimensional color-coded maps. An alternative EBSD plotting scheme known as Quaternions can potentially solve the problem by displaying all of the Euler angle orientation information with a complex dual color-contrast color scheme [56]. The complex color-coding scheme has been difficult for human visualization due to the involvement of less saturated colors and, thus, has received less popularity than the inverse- pole

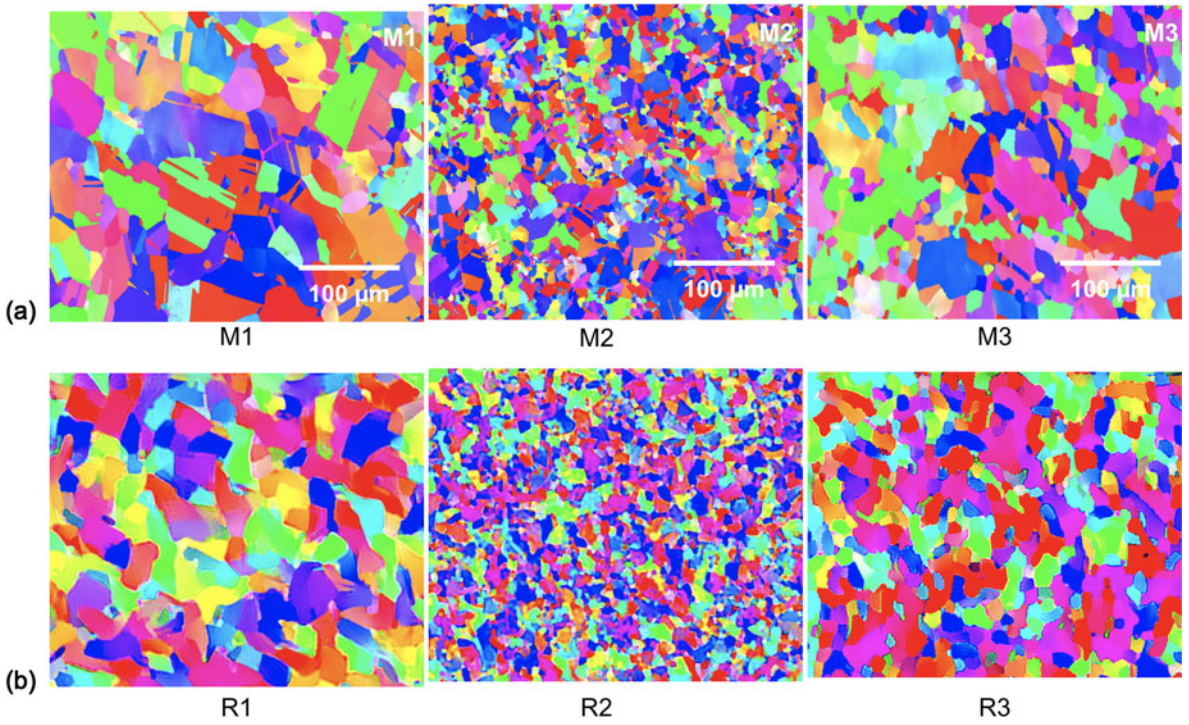

Figure 5: Regenerated microstructures (R1, R2, and R3) based on the Gram matrices from M1, M2, and M3, respectively. (a) Original EBSD measurements and (b) regenerated microstructures. We see that the grain orientation distribution and grain size distribution are preserved for each regenerated microstructure category.

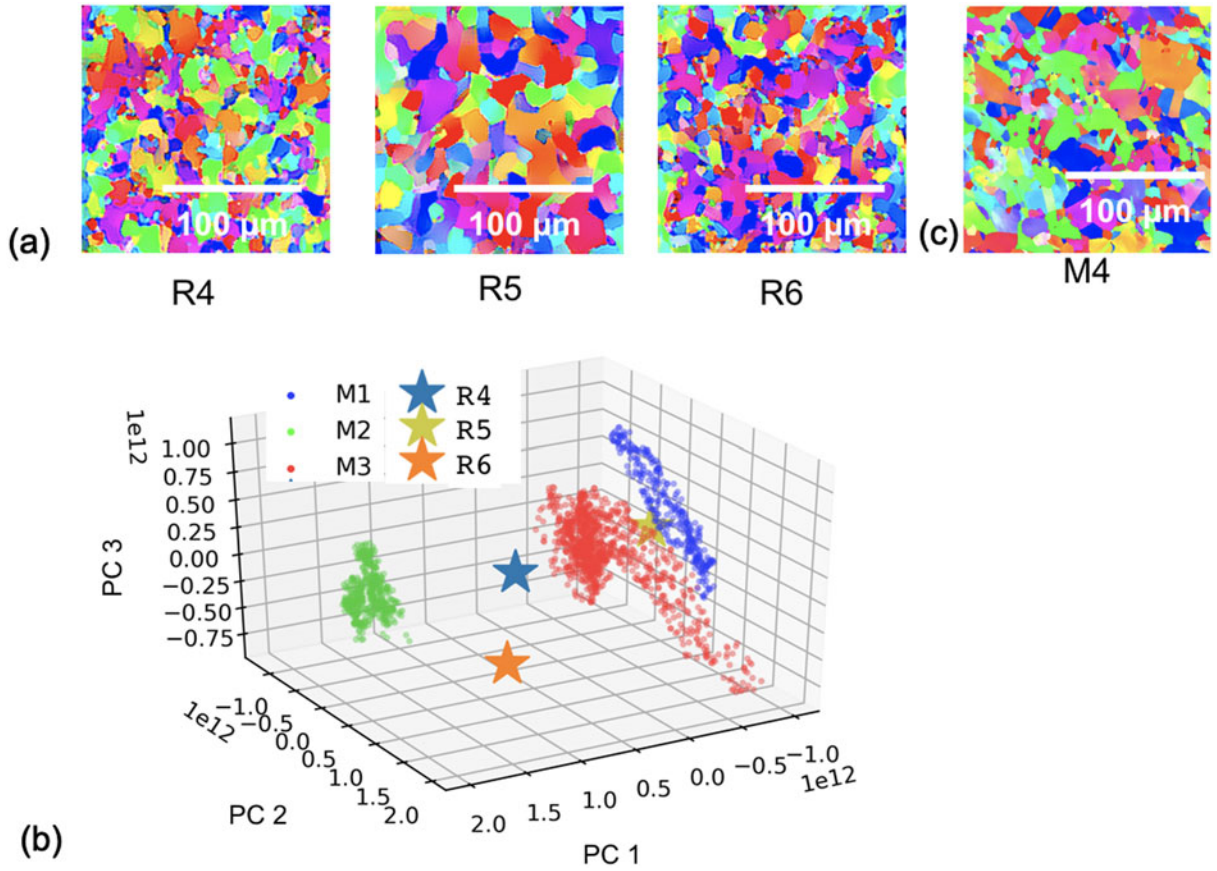

Figure 6: Prediction of microstructures from arbitrary PC values *via* regeneration. (a) Predicted microstructure R4 with PC values set at the centroid location of M4 in Table II, R5 from the middle point between M1 and M3, and R6 from the middle point between M2 and M3. (b) Locations of the predicted microstructure in the reduced domain of the first three PCs. (c) Patch data from the measurement of M4. The similarity between M4 and R4 demonstrates the accuracy of the representation framework.

figure. However, this will not be an issue for machine learning and computer vision. Another notable feature lost in the regenerated microstructures is twinning, which is a characteristic feature in M1. This problem may be addressed by increasing the depth of the DNN to improve the emphasis on the small-scale features. In addition, removing flipped samples from the training data can also be helpful to preserve the twin features in microstructure regeneration, because twin features are not symmetric upon image flipping.

TABLE III. The PC values for regenerated microstructure in Fig. 7.

Indexing	PC1 (10^{11})	PC2 (10^{11})	PC3 (10^{11})	PC4 (10^{11})	PC5 (10^{11})
Row 1A	−15.295	−1.418	−1.174	−0.242	−0.814
Row 1B	−10.033	−1.418	−1.174	−0.242	−0.814
Row 1C	−5.352	−1.418	−1.174	−0.242	−0.814
Row 1D	−0.404	−1.418	−1.174	−0.242	−0.814
Row 1E	4.560	−1.418	−1.174	−0.242	−0.814
Row 2A	−5.352	−29.385	−1.174	−0.242	−0.814
Row 2B	−5.352	−15.401	−1.174	−0.242	−0.814
Row 2C	−5.352	−1.418	−1.174	−0.242	−0.814
Row 2D	−5.352	12.565	−1.174	−0.242	−0.814
Row 2E	−5.352	26.549	−1.174	−0.242	−0.814
Row 3A	−5.352	−1.418	−12.107	−0.242	−0.814
Row 3B	−5.352	−1.418	−6.641	−0.242	−0.814
Row 3C	−5.352	−1.418	−1.174	−0.242	−0.814
Row 3D	−5.352	−1.418	4.292	−0.242	−0.814
Row 3E	−5.352	−1.418	9.758	−0.242	−0.814

CONCLUSIONS

In conclusion, we have presented a deep learning-enabled framework for microstructure representation and regeneration and have demonstrated its effectiveness by examining the microstructures of samples fabricated by a solid-state AM technology: additive friction stir deposition. The most important conclusions from this exploratory study include:

- By analyzing the EBSD patterns through a DNN, we successfully identify and extract a set of principal microstructural descriptors to reveal the most salient changes between the input microstructures. In the example of copper samples processed under different conditions, the difference of microstructures in the processing domain is captured by merely five principal components. The efficiency and

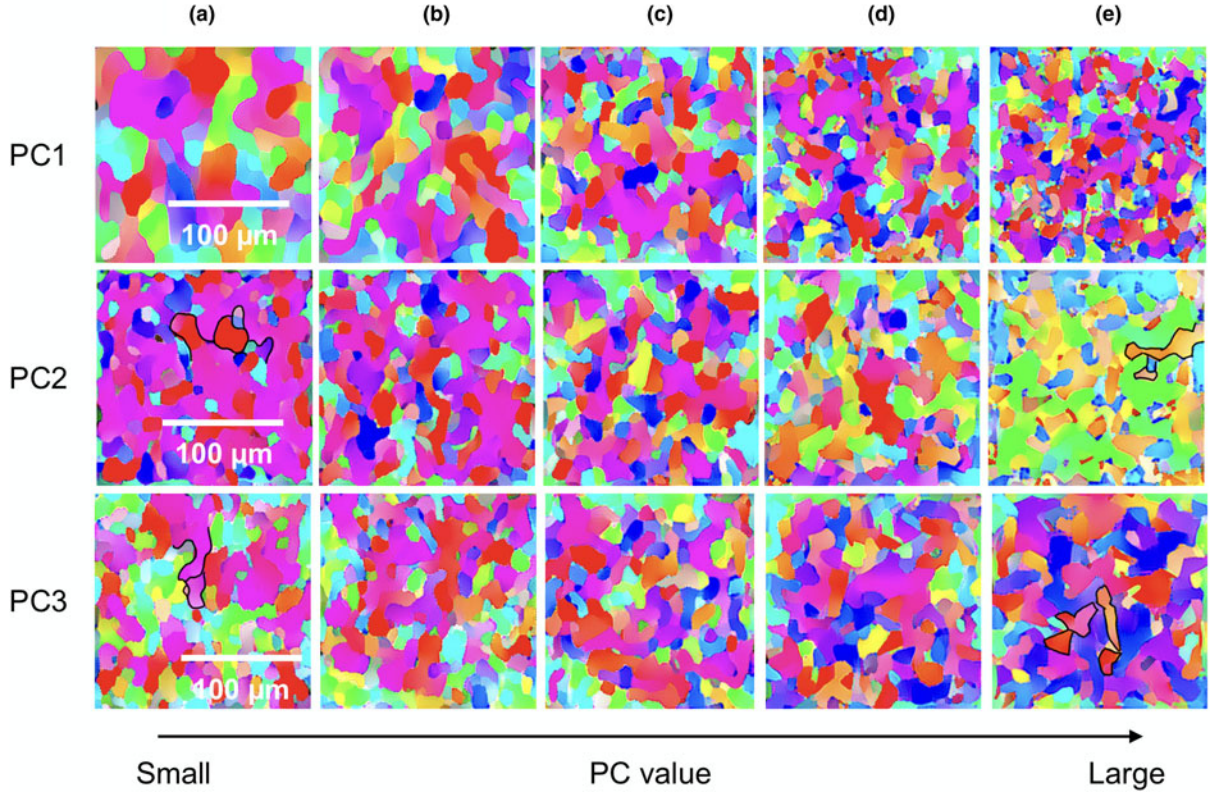

Figure 7: Microstructure evolution with varying principal component values. Starting from the centroid location of M3, microstructures are generated by sequentially stepping along the PC1, PC2, and PC3 axes by −2, −1, 0, 1, and 2 units, respectively. Representative grain boundary morphology in 2A, 2E and 3A, 3E is highlighted. The PC values used to generate these microstructures are summarized in Table III.

accuracy of the established representation are validated by the nearly perfect classification and visually similar regeneration.

- Microstructure regeneration is successfully implemented within the 5D reduced representation domain. This includes both repetition of known microstructures and prediction of "in-between" microstructures at arbitrary locations in the 5D domain.
- The physical meaning of the microstructure descriptors is explored by mapping the regenerated microstructures in the representation domain, wherein the most important descriptors are suggested to correspond to the grain size, grain orientation, and grain boundary morphology.

Quantitative grain orientation analysis can be implemented in the regenerated microstructure by employing more complex color-coding schemes in future works. The presented framework will then enable quantitative trend analysis and microstructure prediction, thereby paving the road toward resolving several core materials science problems, such as microstructural evolution prediction, processing-structure linkage modeling, and heterogeneous material design and optimization.

EXPERIMENTAL PROCEDURES

EBSD data were obtained from Cu-110 and Al 6061 samples fabricated by additive friction stir deposition using an MELD R2 machine (MELD Manufacturing Corporation, Christiansburg, Virginia, USA). Deposition conditions were changed by adjusting the tool rotational velocity and tool travel velocity during deposition. The deposited materials were cut and sectioned in order to examine the cross section in line with the longitudinal direction of the tool during deposition. The imaging was implemented on approximately the same position for each sample, which was in the top layer close to the centerline of the deposit. The samples were electro-polished in preparation for EBSD, which was performed using an FEI Helios 600 NanoLab DualBeam Microscope, Hillsboro, Oregon, USA. The inverse pole figure maps were generated from the EBSD data using the open-source software ATEX [57].

Acknowledgment

Y.Z. gratefully acknowledges the support of the National Science Foundation under Award No. CMMI-1825646.

References

1. **I. Gibson, D.W. Rosen, and B. Stucker**: *Additive Manufacturing Technologies : 3D Printing, Rapid Prototyping and Direct Digital Manufacturing*, 2nd ed. (Springer, New York; London, 2015).
2. **A. Hehr and M. Norfolk**: A comprehensive review of ultrasonic additive manufacturing. *Rapid Protyp. J.* **26**(3), 445–458 (2019).
3. **R.J. Griffiths, M.E. Perry, J.M. Sietins, Y. Zhu, N. Hardwick, C.D. Cox, H.A. Rauch, and Z.Y. Hang**: A perspective on solid-state additive manufacturing of aluminum matrix composites using MELD. *J. Mater. Eng. Perform.* **28**, 648–656 (2019).
4. **H.Z. Yu, M.E. Jones, G.W. Brady, R.J. Griffiths, D. Garcia, H.A. Rauch, C.D. Cox, and N. Hardwick**: Non-beam-based metal additive manufacturing enabled by additive friction stir deposition. *Scr. Mater.* **153**, 122–130 (2018).
5. **A. Yadollahi and N. Shamsaei**: Additive manufacturing of fatigue resistant materials: Challenges and opportunities. *Int. J. Fatigue* **98**, 14–31 (2017).
6. **Z. Wang, T.A. Palmer, and A.M. Beese**: Effect of processing parameters on microstructure and tensile properties of austenitic stainless steel 304L made by directed energy deposition additive manufacturing. *Acta Mater.* **110**, 226–235 (2016).
7. **W.E. Frazier**: Metal additive manufacturing: A review. *J. Mater. Eng. Perform.* **23**, 1917–1928 (2014).
8. **A.J. Schwartz, M. Kumar, B.L. Adams, and D.P. Field**: *Electron Backscatter Diffraction in Materials Science* (Springer, Boston, MA, 2000).
9. **F. Humphreys**: Characterisation of fine-scale microstructures by electron backscatter diffraction (EBSD). *Scr. Mater.* **51**, 771–776 (2004).
10. **T. Maitland and S. Sitzman**: *Electron Backscatter Diffraction (EBSD) Technique and Materials Characterization Examples* (Springer, Berlin, 2007).
11. **J. Mason and C. Schuh**: The generalized Mackenzie distribution: Disorientation angle distributions for arbitrary textures. *Acta Mater.* **57**, 4186–4197 (2009).
12. **J. Mason and C. Schuh**: Hyperspherical harmonics for the representation of crystallographic texture. *Acta Mater.* **56**, 6141–6155 (2008).
13. **O.K. Johnson, J.M. Lund, and T.R. Critchfield**: Spectral graph theory for characterization and homogenization of grain boundary networks. *Acta Mater.* **146**, 42–54 (2018).
14. **D.T. Fullwood, S.R. Niezgoda, B.L. Adams, and S.R. Kalidindi**: Microstructure sensitive design for performance optimization. *Prog. Mater. Sci.* **55**, 477–562 (2010).
15. **S. Patala**: Understanding grain boundaries – The role of crystallography, structural descriptors and machine learning. *Comput. Mater. Sci.* **162**, 281–294 (2019).
16. **J.K. Mason and S. Patala**: Basis functions on the grain boundary space: Theory. arXiv preprint arXiv:1909.11838 (2019).
17. **T. Guo, D.J. Lohan, R. Cang, M.Y. Ren, and J.T. Allison**: An indirect design representation for topology optimization using variational autoencoder and style transfer. In *AIAA/ASCE/AHS/ASC Structures, Structural Dynamics, and Materials. 210049 edn, American Institute of Aeronautics and Astronautics Inc, AIAA, AIAA/ASCE/AHS/ASC Structures, Structural Dynamics, and Materials Conference*, 2018, Kissimmee, United States, 1/8/18.
18. **Y. Chen, H. Jiang, C. Li, X. Jia, and P. Ghamisi**: Deep feature extraction and classification of hyperspectral images based on convolutional neural networks. *IEEE Trans. Geosci. Remote Sens.* **54**, 6232–6251 (2016).
19. **Y. Lv, Y. Duan, W. Kang, Z. Li, and F.-Y. Wang**: Traffic flow prediction with big data: A deep learning approach. *IEEE Trans. Intell. Transp. Syst.* **16**, 865–873 (2014).
20. **X.-W. Chen and X. Lin**: Big data deep learning: Challenges and perspectives. *IEEE Access* **2**, 514–525 (2014).
21. **Y. LeCun, Y. Bengio, and G. Hinton**: Deep learning. *Nature* **521**, 436 (2015).
22. **A. Krizhevsky, I. Sutskever, and G.E. Hinton**: Imagenet classification with deep convolutional neural networks. *Adv. Neural Inform. Process. Syst.* **1**, 1097–1105 (2012).
23. **K. He, X. Zhang, S. Ren, and J. Sun**: Deep residual learning for image recognition. In *2016 IEEE Conference on Computer Vision and Pattern Recognition (CVPR)*, (Las Vegas, NV, 2016); pp. 770–778.
24. **C. Szegedy, W. Liu, Y. Jia, P. Sermanet, S. Reed, D. Anguelov, D. Erhan, V. Vanhoucke, and A. Rabinovich**: Going deeper with convolutions. In *2015 IEEE Conference on Computer Vision and Pattern Recognition (CVPR)*, (Boston, MA, 2015); pp. 1–9.
25. **J. Long, E. Shelhamer, and T. Darrell**: Fully convolutional networks for semantic segmentation. In *2015 IEEE Conference on Computer Vision and Pattern Recognition (CVPR)*, (Boston, MA, 2015); pp. 3431–3440.
26. **W. Liu, D. Anguelov, D. Erhan, C. Szegedy, S. Reed, C.-Y. Fu, and A.C. Berg**: SSD: Single Shot Multibox Detector. In *Computer Vision – ECCV 2016. ECCV 2016. Lecture Notes in Computer Science, vol 9905*, B. Leibe, J. Matas, N. Sebe, and M. Welling, eds. (Springer, Cham, 2016); pp. 21–37.
27. **S. Ren, K. He, R. Girshick, and J. Sun**: Faster R-CNN: Towards real-time object detection with region proposal networks. In *IEEE Transactions on Pattern Analysis and Machine Intelligence*, (vol. 39, no. 6, 2017) pp. 1137–1149.
28. **J. Redmon, S. Divvala, R. Girshick, and A. Farhadi**: You only look once: Unified, real-time object detection. In *2016 IEEE Conference on Computer Vision and Pattern Recognition (CVPR)*, (Las Vegas, NV, 2016); pp. 779–788.
29. **K. He, G. Gkioxari, P. Dollár, and R. Girshick**: Mask R-CNN. In *2017 IEEE International Conference on Computer Vision (ICCV)*, (Venice, 2017); pp. 2980–2988.

30. **S.M. Azimi, D. Britz, M. Engstler, M. Fritz, and F. Mücklich**: Advanced steel microstructural classification by deep learning methods. *Sci. Rep*. **8**, 2128 (2018).
31. **A. Chowdhury, E. Kautz, B. Yener, and D. Lewis**: Image driven machine learning methods for microstructure recognition. *Comput. Mat. Sci.* **123**, 176–187 (2016).
32. **A.R. Kitahara and E.A. Holm**: Microstructure cluster analysis with transfer learning and unsupervised learning. *Integr. Mater. Manuf. Innov.* **7**, 148–156 (2018).
33. **Q. Gao and S. Roth**: Texture synthesis: From convolutional RBMs to efficient deterministic algorithms. In *Structural, Syntactic, and Statistical Pattern Recognition. S+SSPR 2014. Lecture Notes in Computer Science, vol 8621*, P. Fränti, G. Brown, M. Loog, F. Escolano, and M. Pelillo, eds. (Springer, Berlin, Heidelberg, 2014); pp. 434–443.
34. **L. Gatys, A.S. Ecker, and M. Bethge**: Texture synthesis using convolutional neural networks. *Adv. Neural Inf. Process. Syst*. **1**, 262–270 (2015).
35. **R. Cang, Y. Xu, S. Chen, Y. Liu, Y. Jiao, and M. Yi Ren**: Microstructure representation and reconstruction of heterogeneous materials via deep belief network for computational material design. *J. Mech. Des.* **139**(7), 071404 (2017).
36. **R. Liu, A. Kumar, Z. Chen, A. Agrawal, V. Sundararaghavan, and A. Choudhary**: A predictive machine learning approach for microstructure optimization and materials design. *Sci. Rep*. **5**, 11551 (2015).
37. **X. Li, Y. Zhang, H. Zhao, C. Burkhart, L.C. Brinson, and W. Chen**: A transfer learning approach for microstructure reconstruction and structure-property predictions. *Sci. Rep*. **8**, 13461 (2018).
38. **R. Liu, A. Agrawal, W.-K. Liao, A. Choudhary, and M. De Graef**: Materials discovery: Understanding polycrystals from large-scale electron patterns. In *2016 IEEE International Conference on Big Data (Big Data)*, (Washington, DC, 2016); pp. 2261–2269.
39. **K. Kaufmann, C. Zhu, A.S. Rosengarten, D. Maryanovsky, T.J. Harrington, E. Marin, and K.S. Vecchio**: Paradigm shift in electron-based crystallography via machine learning. arXiv preprint arXiv:1902.03682 (2019).
40. **D. Jha, S. Singh, R. Al-Bahrani, W.-K. Liao, A. Choudhary, M. De Graef, and A. Agrawal**: Extracting grain orientations from EBSD patterns of polycrystalline materials using convolutional neural networks. *Microsc. Microanal.* **24**, 497–502 (2018).
41. **T. Karras, S. Laine, and T. Aila**: A style-based generator architecture for generative adversarial networks. In *2019 IEEE/CVF Conference on Computer Vision and Pattern Recognition (CVPR)*, (Long Beach, CA, USA, 2019); pp. 4396–4405.
42. **A. Kirillov, Y. Wu, K. He, and R. Girshick**: PointRend: Image segmentation as rendering. arXiv preprint arXiv:1912.08193 (2019).
43. **N. Lubbers, T. Lookman, and K. Barros**: Inferring low-dimensional microstructure representations using convolutional neural networks. *Phys. Rev. E* **96**, 052111 (2017).
44. **K. Simonyan and A. Zisserman**: Very deep convolutional networks for large-scale image recognition. arXiv preprint arXiv:1409.1556 (2014).
45. **J. Deng, W. Dong, R. Socher, L.-J. Li, K. Li, and L. Fei-Fei**: Imagenet: A large-scale hierarchical image database. In *2009 IEEE Conference on Computer Vision and Pattern Recognition*, (Miami, FL, 2009); pp. 248–255.
46. **G. Mesnil, Y. Dauphin, X. Glorot, S. Rifai, Y. Bengio, I. Goodfellow, E. Lavoie, X. Muller, G. Desjardins, and D. Warde-Farley**: Using Recurrent Neural Networks for Slot Filling in Spoken Language Understanding. In *IEEE/ACM Transactions on Audio, Speech, and Language Processing*, (vol. 23, no. 3, 2015) pp. 530–539.
47. **J. Chi, E. Walia, P. Babyn, J. Wang, G. Groot, and M. Eramian**: Thyroid nodule classification in ultrasound images by fine-tuning deep convolutional neural network. *J. Digit. Imaging* **30**, 477–486 (2017).
48. **M. Abadi, P. Barham, J. Chen, Z. Chen, A. Davis, J. Dean, M. Devin, S. Ghemawat, G. Irving, and M. Isard**: Tensorflow: A system for large-scale machine learning. In *12th {USENIX} Symposium on Operating Systems Design and Implementation ({OSDI} 16)*, (Savannah, GA, USA, 2016); pp. 265–283.
49. **F. Chollet, Keras**: https://github.com/fchollet/keras, 2015.
50. **F. Pedregosa, G. Varoquaux, A. Gramfort, V. Michel, B. Thirion, O. Grisel, M. Blondel, P. Prettenhofer, R. Weiss, and V. Dubourg**: Scikit-learn: Machine learning in Python. *J. Mach. Learn. Res.* **12**, 2825–2830 (2011).
51. **R.J. Griffiths, D. Garcia, J. Song, V.K. Vasudevan, M.A. Steiner, W. Cai, and H.Z. Yu**: Solid-state additive manufacturing of aluminum and copper via additive friction stir deposition: Process-microstructure linkages. (Materialia, 2020). (under review).
52. **C. Cortes and V. Vapnik**: Support-vector networks. *Mach. Learn*. **20**, 273–297 (1995).
53. **J.A. Suykens and J. Vandewalle**: Least squares support vector machine classifiers. *Neural Process. Lett*. **9**, 293–300 (1999).
54. **A. Chambolle**: An algorithm for total variation minimization and applications. *J. Math. Imaging Vis*. **20**, 89–97 (2004).
55. **R.H. Byrd, P. Lu, J. Nocedal, and C. Zhu**: A limited memory algorithm for bound constrained optimization. *SIAM J. Sci. Comput*. **16**, 1190–1208 (1995).
56. **A. Melcher, A. Unser, M. Reichhardt, B. Nestler, M. Pötschke, and M. Selzer**: Conversion of EBSD data by a quaternion based algorithm to be used for grain structure simulations. *Tech. Mech.* **30**, 401–413 (2010).
57. **B. Beausir and J. Fundenberger**: Analysis tools for electron and X-ray diffraction. ATEX software (2017). Available at: www.atex-software.eu (accessed May 22–June 12, 2019).